

# SCIENTIFIC REPORTS

OPEN

## Single-crystalline ZnO sheet Source-Gated Transistors

A. S. Dahiya<sup>1</sup>, C. Opoku<sup>1</sup>, R. A. Sporea<sup>2</sup>, B. Sarvankumar<sup>1</sup>, G. Poulin-Vittrant<sup>3</sup>, F. Cayrel<sup>1</sup>, N. Camara<sup>1</sup> & D. Alquier<sup>1</sup>

Received: 05 October 2015

Accepted: 09 December 2015

Published: 13 January 2016

Due to their fabrication simplicity, fully compatible with low-cost large-area device assembly strategies, source-gated transistors (SGTs) have received significant research attention in the area of high-performance electronics over large area low-cost substrates. While usually based on either amorphous or polycrystalline silicon ( $\alpha$ -Si and poly-Si, respectively) thin-film technologies, the present work demonstrate the assembly of SGTs based on single-crystalline ZnO sheet (ZS) with asymmetric ohmic drain and Schottky source contacts. Electrical transport studies of the fabricated devices show excellent field-effect transport behaviour with abrupt drain current saturation ( $I_{DS}^{SAT}$ ) at low drain voltages well below 2V, even at very large gate voltages. The performance of a ZS based SGT is compared with a similar device with ohmic source contacts. The ZS SGT is found to exhibit much higher intrinsic gain, comparable on/off ratio and low off currents in the sub-picoamp range. This approach of device assembly may form the technological basis for highly efficient low-power analog and digital electronics using ZnO and/or other semiconducting nanomaterial.

The last decade has seen resurgence in the popularity of an already matured field of nanotechnology. This is expected to aid the development of next generation efficient electronic devices incorporating nanostructures. As miniaturization *via* top down approach is nearing its limits for commercial viability, efforts are made to develop new materials with enhanced functionalities as fundamental components in future electronic/optoelectronic devices<sup>1</sup>. Significant developments in the synthesis of functional nanometrials *via* self-assembly from the bottom-up approach<sup>1,2</sup> is now offering high quality materials. Additionally, the discovery and possible isolation of atomic level thick two-dimensional (2D) Graphene sheet has also spearheaded a new revolution in nanomaterial research targeting novel electronic devices and systems<sup>3</sup>. However, the main drawback limiting the widespread use of Graphene is the material zero band-gap<sup>4</sup>. This limitation of Graphene has seen a resurgence in research activities dedicated to other 2D semiconducting nanomaterials such as MoS<sub>2</sub>, WS<sub>2</sub> and ZnO, due to their unique electrical<sup>5,6</sup>, optical<sup>7,8</sup> and magnetic<sup>5,6</sup> properties. While several literature data exists on the charge transport properties<sup>8–13</sup> in such materials, the study of charge transport in single-crystalline ZnO nanosheets (NSs) is still limited<sup>12,13</sup>. This is surprising, since ZnO exhibits number of unique electrical and optical properties such as wide band-gap (3.34 eV), high exciton binding energy (60 meV), excellent thermal stability, and moderate to high electron carrier mobility ( $\sim 200 \text{ cm}^2 \text{ V}^{-1} \text{ s}^{-1}$ ). Unlike other 2D semiconducting materials<sup>14,15</sup>, extraction of atomic layer ZnO is still challenging, although the growth of a few nanometer thick single-crystalline ZnO NSs<sup>5</sup> have been demonstrated using bottom-up approaches. Such 2D ZnO NSs have gained significant attention for applications like: photovoltaics<sup>16</sup>, gas<sup>17</sup>/UV<sup>18</sup> sensors and piezoelectric nanogenerators<sup>19</sup>. Since ZnO in the form of poly-crystalline thin films and single-crystalline nanowires (NWs) has been extensively studied as potential materials for the assembly of high performance field-effect transistors, targeting low-power applications<sup>20–25</sup>, it is envisaged that 2D single-crystalline ZnO NSs could offer additional functionalities in this area of nanomaterial research.

Conventionally, field-effect transistors (FETs) are engineered with ohmic source and drain (s/d) contacts. More recently, a new type of transistors operation has been introduced by Shannon and Gerstner<sup>26</sup>, called “source-gated transistor (SGT)”, which exploited the reverse bias Schottky diode located at the source region with markedly different saturation characteristics to that of conventional FETs with ohmic contacts<sup>26–30</sup>. A schematic of a typical SGT device is shown in Fig. 1. Of significant importance to the successful operation of SGT is the

<sup>1</sup>Université François Rabelais de Tours, CNRS, GREMAN UMR 7347, 16, rue pierre et marie Curie, 37071 Tours, France. <sup>2</sup>Advanced Technology Institute, University of Surrey, Guildford, Surrey, GU2 7XH, United Kingdom. <sup>3</sup>Université François Rabelais de Tours, INSA-CVL, CNRS, GREMAN UMR 7347, 3 rue de la Chocolaterie, CS 23410, 41034 BLOIS Cedex, France. Correspondence and requests for materials should be addressed to D.A. (email: daniel.alquier@univ-tours.fr)

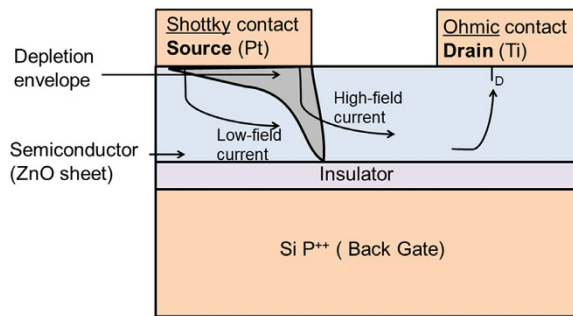


**Figure 1. Cross-sectional device structure of a SGT.** In blue are the materials used in our device. In grey is the depletion envelope at the source under small drain bias showing pinch-off. Current is controlled by the reverse biased Schottky source contact. The total current of the device itself is a contribution of two components, namely, high-field and low-field mode of operation. The high-field mode is through the modulation of barrier height present at the edge of the source while the low-field mode is through the depletion region present under bulk of the source.

configuration of the gate electrode, which must extend across the entire portion of the semiconductor sandwiched by the Schottky source and the gate insulator layer<sup>26</sup>.

Exploitation of stable Schottky source/drain contacts in nanostructure based FETs<sup>31,32</sup> (SB-FETs) have already been performed in the past. However, the device principle of SGTs is greatly different from SB-FETs even though both devices exploit a Schottky barrier at the source contact. The operating principle of the SGT can be ascribed to its geometry, which allows effective manipulation of the depleted region in the semiconductor near the vicinity of the Schottky source by the gate field (with applied gate voltage,  $V_{GS}$ ). In contrast to conventional FETs, the SGT exploits the reverse bias Schottky barrier at the source to afford much lower saturation voltages even at high gate voltages. This effect leads to several advantages, some of which includes: (i) early drain current saturation<sup>26,28,33</sup> with the drain voltage ( $V_{DS}$ ), (ii) immunity of drain current ( $I_{DS}$ ) to channel length variations<sup>33</sup>, and (iii) possible immunity to short-channel effects<sup>30</sup>. This key defining feature of the SGT could be ideal in the design of low-power electronics, where fast switching is not necessarily a key objective.

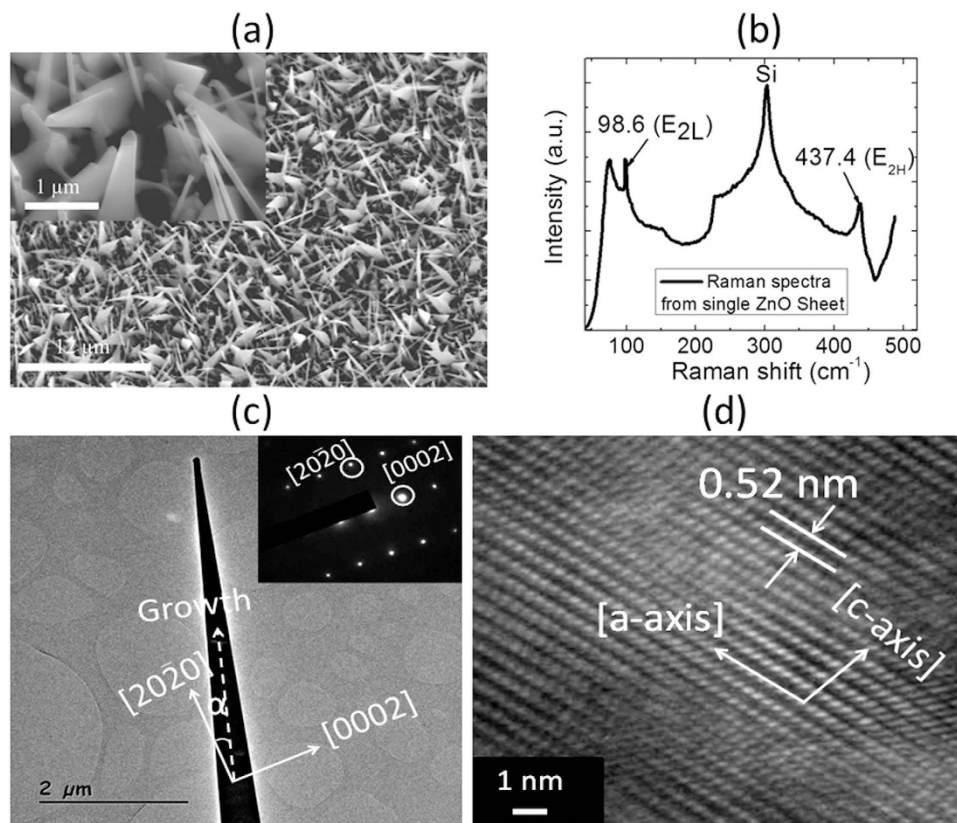
The design of SGTs have been realized in a few semiconducting modules, namely, amorphous Si ( $\alpha$ -Si)<sup>28</sup>, poly-crystalline Si (poly-Si)<sup>27,34</sup> and poly-crystalline ZnO<sup>22,23</sup>. However, almost no data exist on the use of nanostructures or single crystals as active semiconducting modules in SGT assembly. In this work, we demonstrate fully operational SGTs based on single-crystalline ZnO sheets (ZSs), which to the best of our knowledge, has not been reported so far. Detailed discussions will be centred around the ZS growth, nanomaterial characterization and the assembly of single-crystalline ZS based SGTs. Finally, detailed electrical transport studies for the fabricated devices will be presented as follows: Schottky barrier height evaluation, field-effect transport, mobility extraction and the modes of SGT operation.

## Results

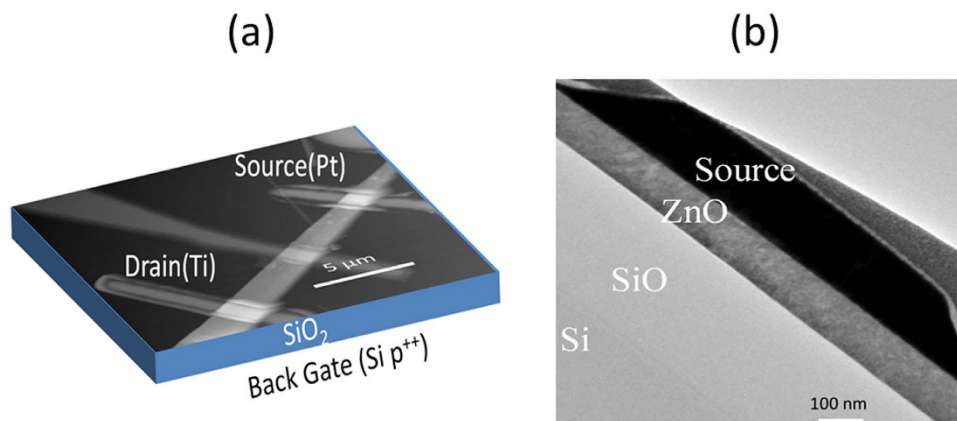
**Material structural characterizations.** To assess the quality of the materials produced, we employed SEM, Raman spectroscopy, and HRTEM, as shown in shown in Fig. 2. Figure 2a shows a typical SEM image of as-grown ZS on Au-coated Sapphire substrate. The ZSs have a triangular shape and their lengths were deduced from assessment of SEM images to be around  $5\ \mu\text{m}$  after 60 min of synthesis. Much longer ZS on the order of  $25\ \mu\text{m}$  were obtained after 180 min of synthesis<sup>13</sup>. To determine the crystal quality and orientation of as-grown ZSs, micro-Raman and HRTEM measurements were performed. The room temperature Raman scattering was observed by a confocal microscope ( $\times 100$  objective) using a  $514.5\ \text{nm}$  polarized line. The diameter of the resulting laser spot was around  $1\ \mu\text{m}$ , which was much smaller than the dimensions of the single ZS deposited on oxide. From this Raman data (Fig. 2b), the two dominant peaks centred at  $98.6$  and  $437.4\ \text{cm}^{-1}$  correspond only to investigated single ZS. These peaks are assigned to the two nonpolar first-order Raman active  $E_2$  (low) and  $E_2$  (high) modes, corresponding to the Raman selection rule of wurtzite ZnO (with  $C_{6v}$  point group symmetry). These  $E_2$  modes are dominating the Raman scattering spectra<sup>35</sup>, in accordance with a high crystal ZS material, as confirmed by the very small values of full width half maximum (FWHM) of the measured peaks:  $2.2$  and  $5.4\ \text{cm}^{-1}$ , respectively. Finally, HRTEM characterizations were performed on single ZS to determine the ZS's atomic structure. Figure 2c shows the low magnification HRTEM image, which was used to determine the as-grown ZS growth direction. A magnified HRTEM image of the ZS (Fig. 2c) is shown in Fig. 2(d). From this image, we were able to determine both the growth direction and other crystallographic orientation of the ZS. The data show that, the lattice fringes along the direction perpendicular to the ZS length, measured to be around  $0.52\ \text{nm}$ , corresponding to the  $[0001]$  plane of the wurtzite ZnO crystal.

Figure 3 shows a typical ZS SGT device images. Shown in Fig. 3a is a typical ZS SGT device (based on the superposition of ZS SGT schematic and AFM image). The cross-sectional TEM image of the Schottky contacted source for a representative device is shown in Fig. 3b. From this image, the Pt/n-ZS/SiO<sub>2</sub>/p<sup>++</sup>-Si stack, essential for successful SGT operation, is clearly revealed.

**Electrical characterizations.** *Pt/n-ZnO Schottky Barrier characterization at  $V_{GS} = 0\ \text{V}$ .* The electrical transport characteristics attained by a representative device (shown in Fig. 3a) and a schematic showing a



**Figure 2.** (a) SEM image of the as-grown ZSs on Sapphire substrate. The inset is high-magnification image of the respective sample. (b) Raman spectra measured from single ZS. (c) HRTEM image of single ZS showing the growth direction. The growth direction is always inclined with angle  $\alpha$  to the a-axis. The Inset selected area electron diffraction (SAED) pattern further confirms the single-crystalline nature of the ZS. (d) HRTEM image of ZS.



**Figure 3.** Schematic/AFM image of the ZS SGT device (b) Cross-sectional TEM image of the fabricated SGT device on 290 nm thick  $\text{SiO}_2$  showing the SGT's staggered structure and ZS's approximate thickness of 120 nm.

simplified energy band diagram of the Schottky source contact region for a ZS SGT device with  $W/L$  of around 1.3/9.7  $\mu\text{m}$  are shown in Fig. 4. The temperature dependent  $I-V$  measurements were performed between 303 K and 383 K in the absence of the gate field (i.e.  $V_{\text{GS}} = 0 \text{ V}$ ). The resulting  $I_{\text{DS}}-V_{\text{DS}}$  progressions are shown in Fig. 4a. From these experimental data, it can be seen that the device demonstrates clear rectification behaviour within the measured temperature range. At RT, a rectification ratio ( $\text{RR} = I_{\text{DS}}(-5 \text{ V})/I_{\text{DS}}(+5 \text{ V})$ ) of around 100 is calculated and a reverse saturation current  $I_{\text{DS}}^{\text{SAT}}$  of  $\sim 25 \text{ nA}$  is obtained at  $V_{\text{DS}} = +5 \text{ V}$  in the present device. The Arrhenius plot for SBH extraction is shown in Fig. 4b at  $V_{\text{DS}} = +1.5 \text{ V}$ . To evaluate the effective barrier height at the source Schottky Pt/n-ZnO interface, we used the pure thermionic emission (TE) model to describe the charge carrier transport; as shown in Eq. (1)

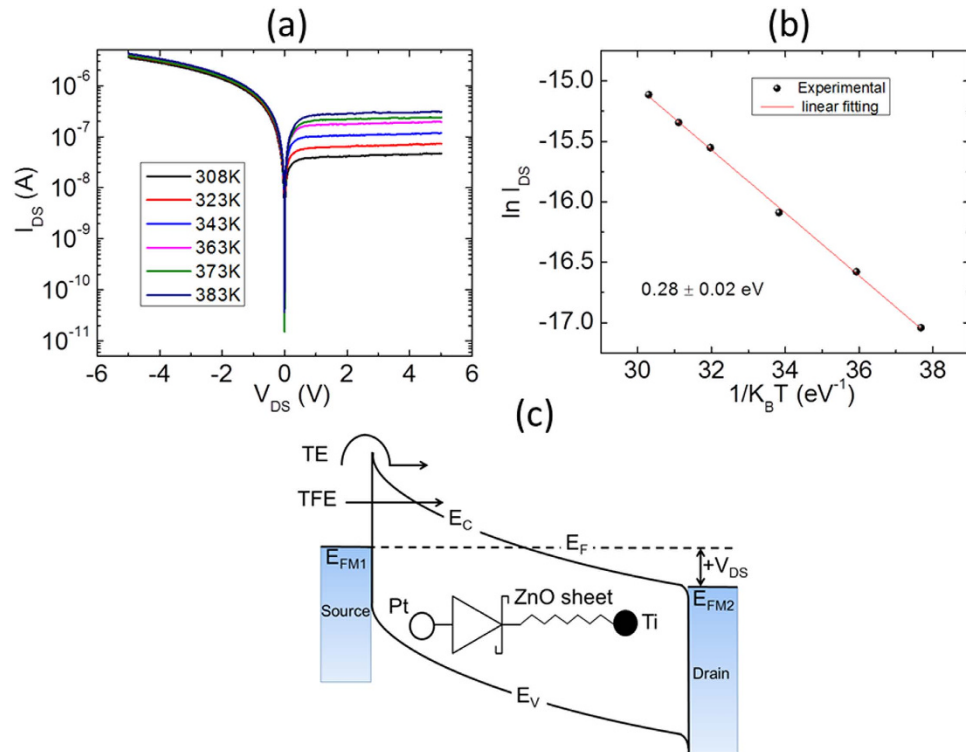


**Figure 4.** (a) I–V characteristics of Pt–ZnO contact as a function of temperature from 308 to 383 K. (b) Arrhenius plot. The activation barrier energy is extracted from the plot by measuring the slope of the curve which comes to be  $0.28 \pm 0.02$  eV. (c) Simplified energy band diagram for Pt–ZnO–Ti system under thermal equilibrium at positive  $V_{DS}$ . Also schematically showing the two dominant charge carrier injection mechanism (TE and TFE) at reverse biased Schottky contact.  $E_{FM1}$  and  $E_{FM2}$  are the Fermi level for metals Pt and Ti, respectively.

$$I_{DS} = A^* S T^2 e^{-\left(\frac{q\phi'_{SB}}{k_B T}\right)} \left( e^{-\left(\frac{qV_D}{nk_B T}\right)} - 1 \right) \quad (1)$$

where  $I_{DS}$  is the drain-to-source current of the ZS device,  $A^*$  is Richardson constant corresponding to the effective mass of electrons in semiconducting ZnO,  $S$  the effective contact area,  $T$  is temperature in Kelvin,  $\phi'_{SB}$  is the effective Schottky barrier height (SBH) and  $k_B$  is Boltzmann's constant ( $\sim 8.617 \times 10^{-5}$  eV K $^{-1}$ ). Using this model, the effective SBH,  $\phi'_{SB}$  can be extracted by performing temperature-dependent  $I_{DS}$ – $V_{DS}$  measurements. Note that since  $A^* \propto 1/ST^2$ , the slope  $\ln\{(\Delta I_{DS})/\Delta(1/k_B T)\}$  from the Arrhenius plot of the current progression gives activation energy ( $E_a$ ). From this data, an activation energy was calculated from the slope of the  $I_{DS}$  progression to be  $\sim 0.28 \pm 0.02$  eV, which is regarded as the effective  $\phi'_{SB}$  at the reverse biased Schottky barrier source diode. Moreover, for statistical assessment of typical SBH that can be expected in such device systems, we also extracted the effective SBH from 10 separate devices under identical experimental conditions to be in the range of 0.24 to 0.44 eV. Notably, these values are significantly lower than reported data for bulk Pt/n-ZnO Schottky contacts (0.72 eV)<sup>36</sup>, but still comparable to the reported data for single-crystalline ZnO nanowire Pt/n-ZnO (0.42 eV) contacts<sup>37</sup>. The differences between the calculated barrier height and those expected in ideal and/or bulk systems from the literature may be partly explained by our approximation of pure thermionic emission. In fact, the reverse bias current is expected to be the result of several charge transport processes at the Pt/n-ZnO interface, including: (i) recombination in depleted region of the ZS, (ii) quantum mechanical tunnel effect below the top of the barrier such as the thermionic field emission (TFE)<sup>38,39</sup>, (iii) barrier lowering due to image force effects<sup>38</sup>, and (iv) Fermi level pinning as a result of surface states and/or source metal–ZnO interface reactions. The combined effects of these mechanisms are expected to contribute to the injection/extraction of charge carriers at the Pt/n-ZS interface. For clarity, we show in Fig. 4c, a simplified energy band diagram of the various mechanisms resulting in the measured  $I_{DS}$  in our devices.

As a result of the successful SBH extraction, numerical simulations for our SGTs structures were performed using Silvaco Atlas, according to ref. 25. We use material parameters for unintentionally doped ZnO thin film<sup>40</sup>. For this investigation, a nominal Schottky barrier height of  $\Phi_{SB}$  zero = 0.28 eV was assumed and the barrier lowering parameters  $\alpha$  and  $\gamma$  were taken to be  $\sim 4$  nm and 0.87, respectively (where SBH  $\Phi_{SB}$  effective =  $\Phi_{SB}$  zero –  $\alpha E_v$ )<sup>28</sup>. The results from these simulations are discussed in the following part of the present work.

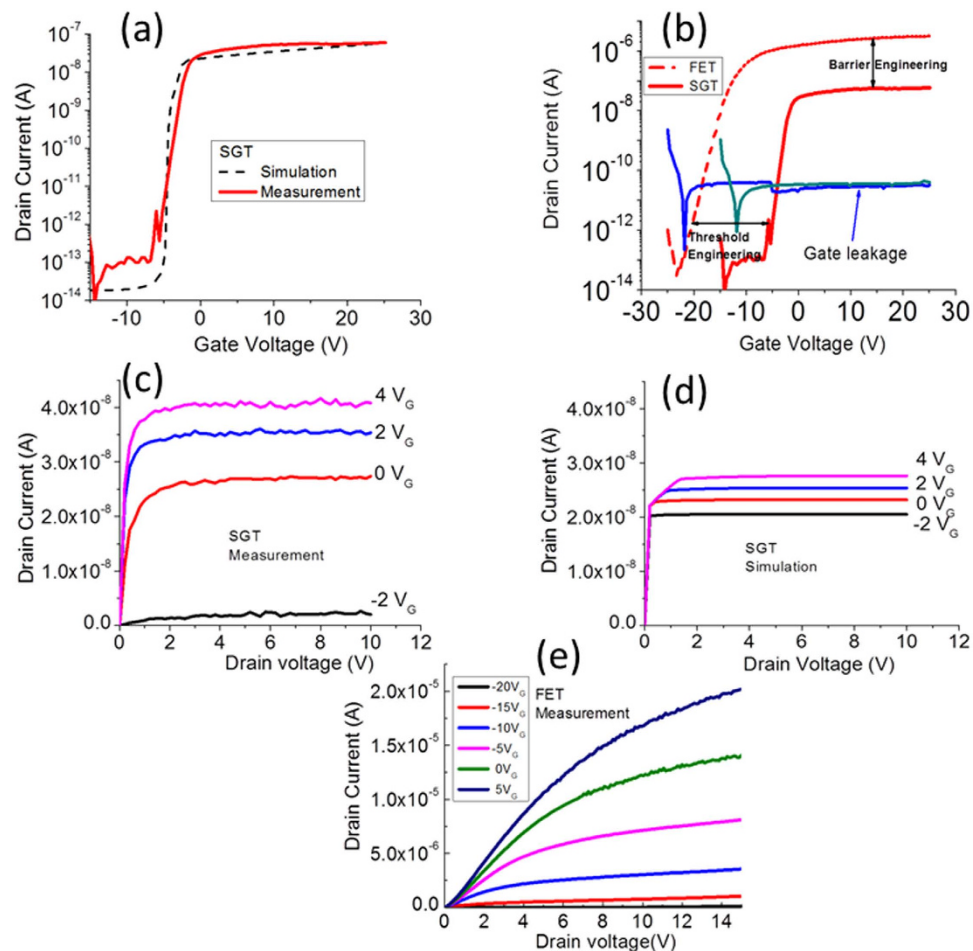


**Figure 5.** (a) Experimental and simulated  $I_{DS}$ - $V_{GS}$  curve of the SGT device at  $V_{DS} = 1$  V. (b)  $I_{DS}$ - $V_{GS}$  curves from the Pt-ZnO (SGT) and Ti-ZnO (FET) curves of the same device at  $V_{DS} = 1$  V. Panel (b) also show the gate leakage current for both devices. (c) Experimental and (d) simulated output characteristics for the SGT device with  $V_{GS}$  steps of 2 V between  $-2$  to 4 V. (e) Output characteristics for the FET device with  $V_{GS}$  steps of 5 V between  $-20$  to 5 V.

**General field-effect characteristics: threshold voltage, leakage current, sub-threshold swing, current on/off ratio, mobility.** The general field-effect characteristics exhibited by both devices: (i) a ‘standard’ FET with ohmic contacts and (ii) a SGT with Schottky source contact will now be discussed to highlight their main differences. It is worth to note that, in order to avoid any effect from different field by applying same  $V_{DS}$  in the device channel, we measured the same device with asymmetric ohmic drain and Schottky source contacts by appropriate biasing for both FET (drain grounded) and SGT (source grounded). In SGT theory, the gate field serves two purposes. Firstly, it modulates the channel conductivity such that a conduction path exists at  $V_{GS} \geq V_{TH}$  for charge transport, as in conventional FET. Secondly, it modulates the SBH by penetrating into the semiconductor region sandwiched by the source and gate electrode<sup>26–28</sup>. As we show in subsequent sections of this work, this key defining differences leads to markedly different transport in such devices.

Experimental and numerical transfer  $I_{DS}$ - $V_{GS}$  scans at constant drain bias ( $V_{DS} = +1$  V) for  $V_{GS}$  bias range of  $-25$  V to 25 V are shown in Fig. 5a,b for both device types. In both cases, the general progression of  $I_{DS}$ , which increases with  $V_{GS}$  bias, is typical of n-channel accumulation mode behaviour. A turn-on voltage of  $\sim -6$  V and  $\sim -22$  V is obtained for the SGT and FET devices, respectively. A linear extrapolation of  $I_{DS}$ - $V_{GS}$  (not shown) revealed threshold voltages ( $V_{TH}$ ) of  $\sim -3.4$  V (SGT) and  $\sim -12$  V (FET). From the semi-log plot of the transfer scans, comparable subthreshold swing  $\approx [\Delta \log I_{DS} / \Delta V_{GS}]$  of  $\sim 750$  mV/dec was obtained in the two device types. From the logarithmic ratio of the on-to-off currents ( $\log_{10} [I_{on} / I_{off}]$ ), an on/off ratio of  $\sim 10^5$  (SGT) and  $\sim 10^7$  (FET) were obtained. The comparatively higher on/off value in the FET is expected due to the absence of a reverse bias Schottky barrier in this device. Notably, both devices demonstrate exceptionally low off state currents in the sub-picoamp ( $\sim 0.1$  pA). Such low currents may be attributed to the use of ohmic drain contact<sup>22</sup> and/or the low free charge carrier density in the ZS used. The field-effect mobility in both devices were evaluated from the standard MOSFET model in the linear regime, as shown in Eq. 2.<sup>41</sup>,

$$\mu_{FE} = \frac{L}{W} \frac{g_m}{C_{OX} V_{DS}} \quad (2)$$

where  $L$  is the channel length,  $W$  the channel width,  $g_m$  the transconductance  $= \partial I_{DS} / \partial V_{GS}$  and  $C_{OX}$  the gate capacitance ( $= \epsilon_0 \epsilon_r / d$ ). From Eq. 2, we obtained a conservative estimation for the field-effect mobility ( $\mu_{FE}$ )  $\sim 5 \text{ cm}^2/\text{Vs}$  (SGT) and  $\sim 50 \text{ cm}^2/\text{Vs}$  (FET) for the devices. It should be noted that the extracted  $\mu_{FE}$  can be regarded as an effective mobility ( $\mu_{eff}$ ) as it does not reflect the true mobility of a contact controlled device such as the present SGT. As such, the mobility of  $5 \text{ cm}^2/\text{Vs}$  is provided purely for comparison. Nonetheless,  $\mu_{eff}$  value in the present ZS SGTs is still higher than that in reported data for other SGT device structures based on poly-ZnO<sup>22,23</sup>. Another important feature to note from the general progression of the  $I_{DS}$  (transfer scans, Fig. 5b), is their markedly different shapes. The SGT shows abrupt current saturation behaviour while for the FET shows much weaker saturation. These differences in operation can be seen much more clearly in the family of output scans for the two devices (Fig. 5(c,e)), in which the SGT shows abrupt  $I_{DS}^{SAT}$  of less than 2 V ( $V_{DS}$ ) even at high  $V_{GS}$  biases. The FET, on the other hand, shows very weak  $I_{DS}^{SAT}$  behaviour. Such differences in the two device types can be directly attributed to the existence of the reverse bias Schottky barrier in the SGT which essentially controls charge carrier injection from contact-to-channel, irrespective of channel conductance (at  $V_{GS} \geq V_{TH}$  and  $V_{DS} \geq V_{DS}^{SAT}$ ).

**Abrupt current voltage saturation/Intrinsic Gain.** The measured and simulated output characteristics ( $I_{DS}$ - $V_{DS}$ ) for the present SGT and FET are depicted in Fig. 5c–e. Notably, the output scans demonstrate excellent modulation with increasing steps of  $V_{GS}$  from  $-2 \text{ V}$  to  $+4 \text{ V}$ . Consistent with the progression of the transfer scans, the SGT output scans also demonstrate abrupt current saturation characteristics with increasing  $V_{GS}$ . Beyond  $V_{DS} = V_{DS}^{SAT}$ ,  $I_{DS}$  is clearly shown to remain fairly stable, invariant with increasing  $V_{DS}$  beyond saturation. Compared to the FET device (Fig. 5(e)), drain current saturation in the SGT device appears at significantly lower drain voltages, even at relatively high gate voltages. In conventional FETs with ohmic contacts, drain current saturation is expected to occur first at the drain end of the channel. This is described by the gradual channel approximation model:  $V_{DS}^{SAT} \approx [V_{GS} - V_{TH}]$ . According to the theory, the ratio of the change in the saturation voltage with gate voltage would be close to unity ( $\partial V_{DS}^{SAT} / \partial V_{GS} \approx 1$ ) for FETs. This is completely different for the SGT device where a  $\partial V_{DS}^{SAT} / \partial V_{GS} \approx 0.1$  was obtained. This is a direct consequence of the small positive drain bias that leads to strong pinch-off near the vicinity of the reverse bias source Schottky contact (see Fig. 1). Beyond this pinch-off point, the supply of charge carriers from source to drain is all but dominated by quantum mechanical tunnelling through the reverse biased Schottky barrier and effective manipulation of the SBH by the gate field acting on it. Moreover, as can be seen from the output scan in Fig. 5c, the progression of  $I_{DS}^{SAT}$  demonstrates a near-linear relationship with incremental increase of  $V_{GS}$  from  $V_{GS} = 0 \text{ V}$  up to  $V_{GS} = 4 \text{ V}$ . Since the physical length of the channel in the SGTs is not expected to play a significant role in charge transport at  $V_{GS} \geq V_{TH}$  and  $V_{DS} \geq V_{DS}^{SAT}$ <sup>27</sup>, we can conclude that SBH lowering is the primary mechanism which controls the increase of  $I_{DS}$  with increasing  $V_{GS}$ . In the following sections, we also show that the barrier height become less sensitive to the gate field beyond a certain  $V_{GS}$  value (typically  $\gg V_{TH}$ ), as in the case of SGT operation in the low field regime<sup>30</sup>.

The features of our device with Schottky source contacts strongly resembles that of a classical SGT<sup>26</sup>, which was shown to offer enhanced performance of transistors targeting logic circuits as well as simple pixel switches in actively addressed liquid-crystal displays. A crucial parameter for most transistor applications is the intrinsic gain  $A_v$ , defined as  $A_v = g_m / g_d$  (where  $g_d = \partial I_{DS} / \partial V_{DS}$ )<sup>42</sup>. The value of  $A_v$  is related to the output impedance<sup>42</sup>. Generally, in conventional FETs with ohmic contacts, high  $A_v$  values are difficult to achieve at low drain voltages unless sufficient  $V_{DS}$  bias ( $\gg V_{DS}^{SAT}$ ) is applied at the drain for drain pinch-off. As shown for the SGTs, much higher  $A_v$  is anticipated, as  $I_{DS}^{SAT}$  occurs first at the source end of the device at significantly lower  $V_{DS}$  biases. This leads to an  $A_v$  higher than 100 at  $V_{DS} = 2 \text{ V}$ , approximately 1000 times higher than in our FET devices. It must be noted that such an abrupt current-voltage saturation and high intrinsic gain characteristics exhibited by our SGTs is expected to be useful in applications where high output impedance, good current uniformity and stability are required, such as in driver transistors in emissive pixel circuits. This is mainly because such devices generally operate in saturation to provide constant currents with some tolerance in supply voltage variations<sup>29</sup>.

## Discussion

The specific mechanism leading to charge carrier transport from contact-to-channel in our ZS SGTs can be analysed in detail by assessing the progression of the transconductance  $g_m$  vs.  $V_{GS}$ , as shown in Fig. 6a. The general trend of  $g_m$  shows a maximum value of 14 nS at  $\sim V_{GS} = -1.5 \text{ V}$ , which then falls abruptly to around 3 nS at  $V_{GS} = 1 \text{ V}$ . Similar to reported data from the literature for SGTs, the behaviour of  $g_m$  can be attributed to the two dominant charge carrier transport processes (TE and TFE)<sup>39</sup> at the metal-semiconductor junction (Pt/n-ZS in the present case). The process of charge carrier injection/extraction at the interface can be well described by the gate potential variation at the ZS-SiO<sub>2</sub> dielectric interface. In the case of a device with large global back gate, the gate potential variation can be expressed by<sup>39,43</sup>:

$$\frac{d^2 \phi(x)}{dx^2} - \frac{\phi(x) - V_G + V_{bi}}{\lambda^2} = - \frac{q(\rho \pm N)}{\epsilon_0 \epsilon_{ZnO}} \quad (3)$$

$$\lambda = \sqrt{\frac{\epsilon_{ZnO} t_{ZnO} t_{OX}}{\epsilon_{OX}}} \quad (4)$$

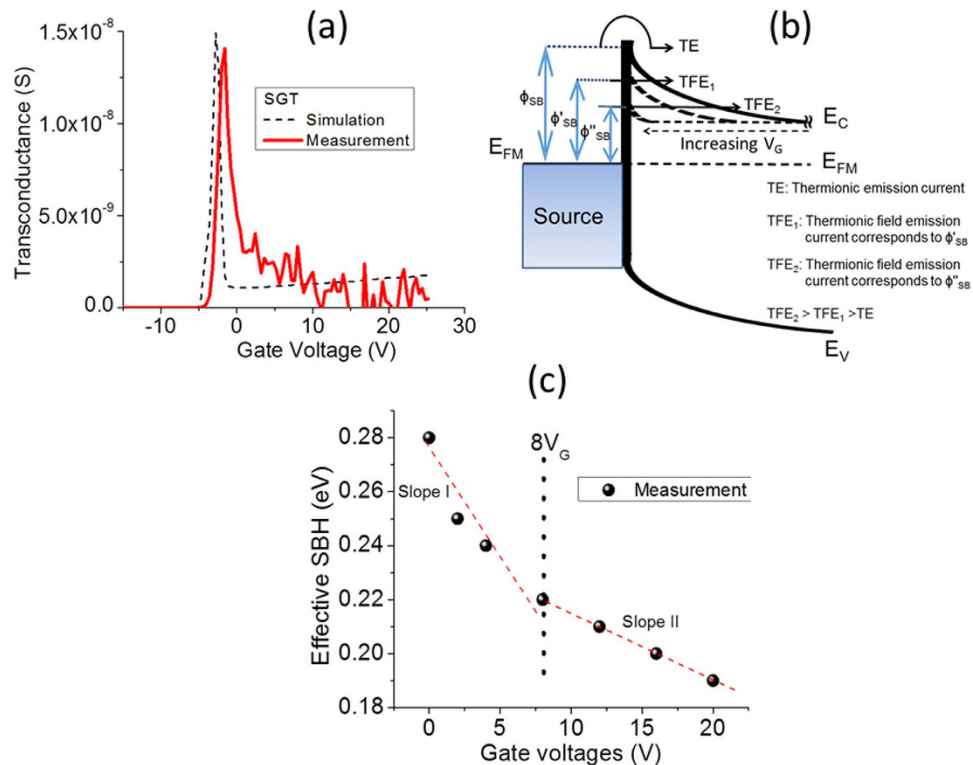


**Figure 6.** (a) Experimental and simulated transconductance curve of the SGT device at  $V_{DS} = 1$  V. (b) Simplified energy band diagram showing variation in effective barrier height with change in applied  $V_{GS}$ . (c) Extracted effective SBH with gate voltage variation when  $V_{DS} = 2$  V. It can be seen that the effective SBH decreases very sharply with rate  $0.007$  eV/ $V_{GS}$  till  $V_{GS}$  equal to  $8$  V (slope I). As shown in (c), beyond  $8$   $V_{GS}$ , SBH demonstrates exceptionally low decrease rate  $0.0024$  eV/ $V_{GS}$  (slope II), which is approximately three times lower than SBH decrease rate below  $8V_{GS}$ .

where  $\Phi(x)$  represents the potential variation at the ZS channel-SiO<sub>2</sub> dielectric interface,  $V_{bi}$  is the built-in potential in the depletion region, directly adjacent to the Pt/n-ZnO interface,  $\rho$  is the density of mobile carriers,  $N$  is constant charge due to ionized donors/acceptors;  $t_{ZnO}$  and  $t_{OX}$  are the thicknesses of ZS and SiO<sub>2</sub>, respectively,  $\lambda$  on the other hand can be regarded as the screening length and/or a scaling parameter. In SGTs, increasing the gate field effectively modulates the width of the depletion region in the semiconductor, provided that:  $V_{GS} \geq V_{TH}$  and  $V_{DS} \geq V_{DS}^{SAT}$ . Increasing gate field modifies the Schottky barrier in such a way that charge carrier injection at the reverse bias Schottky diode is dominated by TFE. However, note in the experimental data (Fig. 6a) that  $g_m$  in the present SGT demonstrates negligible increase beyond a local maxima ( $14$  nS at  $V_{GS} = -1.5$  V). This behaviour of the device presumably suggests that the gate no longer act strongly on the reverse bias source Schottky barrier. In fact, this contradicts the majority of reported data on SGT operation<sup>26,29,34</sup>, whereby the  $g_m$  is expected to increase slowly beyond the local maxima. According to Shannon *et al.*<sup>30</sup>, this can be related to a different operating regime of the SGT. In fact, computational simulation performed by the authors have revealed that the SGT can operate under two distinctive regimes that can be characterized by “high-field and low-field” modes (see Fig. 1).

The high-field operation has been suggested as being the more classical operating mode of the device, in which a greater proportion of the charge (from source to drain) originate from the edge of the source (high-field region). Under this regime  $g_m$  is expected to increase gradually with increasing  $V_{GS}$  even after the observed local maxima. In general, the SBH lowering is exponentially proportional to gate-field. The high-field mode can be explained using the schematic shown in Fig. 6b. From this Figure, at  $V_{GS} > V_{TH}$ , the semiconductor channel is accumulated by charge carriers thus making it more conductive than the reverse bias Schottky diode, provided that sufficient  $V_{DS}$  is applied at the drain (with respect to a grounded source) to ensures that pinch-off occurs first at the source end of the device. Under such biasing conditions, the supply of charge carriers from source in to channel is expected to be dominated by a combination of TFE and image force barrier lowering (at  $V_{GS} > V_{TH}$ ). This regime can be regarded as the high-field and thus, the total source current is expected to be mainly due to the injection of charge carriers at the edge of the source contact. This effect gives an exponential increase of  $I_{DS}$  in the transfer characteristics<sup>30</sup>. However, under low-field mode, a greater proportion of  $I_{DS}$  originates from the injection of charge beyond the edge of the source (low-field region). Due to this, modulation of the SBH by the gate field is negligible. This mechanism may in part explain the low field dependence of the SBH at higher  $V_{GS}$  values from the experimental data. In low-field mode, the source current at low  $V_{GS}$  is expected to steadily increase with  $V_{GS}$  up to a local maximum. However, beyond this local maximum, the source is no longer able to supply sufficient carriers to the channel, resulting in complete  $I_{DS}$  saturation. This is in fact what can be observed in the experimental data shown in Fig. 5a, where  $I_{DS}$  shows negligible increase at  $V_{GS} > \sim 8$  V. The conditions proposed by Shannon *et al.*<sup>30</sup>

for low-field regime include the presence of low SBH and large source-semiconductor overlaps. The source length (2  $\mu\text{m}$ ) and the calculated SBH in the present SGT device (0.28 eV) satisfies the proposed SGT conditions<sup>29,30</sup> in the present work. In an attempt to elucidate the gate field-dependent SBH lowering hypothesis, we carried out temperature-dependent output measurements of our device at gate bias voltages ranging from 0 to 20 V. The results from the temperature work are shown in Fig. 6c. From this experimental data, it can be seen that the effective SBH demonstrates exceptionally low decrease with increasing  $V_{\text{GS}}$  beyond 8 V. Based on experimental observations from Fig. 6c and the general progression of  $g_{\text{m}}$  (Fig. 6a), it is reasonable to conclude that the present device operates in the low-field SGT mode. It has been shown, both by experimental and simulation work<sup>44,45</sup>, a device operating under low-field regime has advantage of having lower activation energy (low temperature dependence) while maintaining the obvious advantages of SGTs such as low saturation voltage and high output impedance in saturation.

## Methods

**ZnO sheet growth procedure.** High density of single-crystalline ZSs were obtained using a catalytic-assisted vapour-liquid-solid (VLS) process in a conventional tube furnace on a Au-coated Sapphire substrates at 950 °C<sup>13</sup>. To grow the ZSs, the source material (ZnO and C at 1:1 weight ratio) was first placed in an Alumina boat, which was subsequently inserted close to the centre of the quartz tube furnace. An Ar ambient was maintained inside the growth chamber throughout the whole process. To initiate the growth, the furnace was ramped to 950 °C at a ramp rate of 30 °C min<sup>-1</sup>, while the growth time at the plateau (950 °C) was varied from 60 to 180 min. After the growth, the furnace was switched off and left to cool naturally to room temperature and growth substrates were recovered thereafter.

**Morphological and structural characterizations.** Morphological and structural characterizations of the as-grown ZSs have been performed in three different equipments. First, a dual beam FEI Strata 400 (FEI, Hillsboro, OR, USA), a focused ion beam (FIB) coupled to a scanning electron microscopy (SEM) system, has been used. It is equipped with a flip stage, a scanning transmission electron microscopy (STEM) detector, and an energy-dispersive x-ray spectroscopy for sample transfer, observation, and elemental composition characterization, accordingly. Furthermore, ZS FET device lamellas have been prepared using the FIB mode and then characterized in STEM mode, but also in second equipment: a high-resolution transmission electron microscopy (HRTEM) using a JEOL 2100 F (JEOL Ltd., Akishima-shi, Japan) operating at an accelerating voltage of 200 kV is performed.

**ZS based transistor fabrication.** To fabricate the ZS SGT/FET devices, the as-grown ZSs were dispersed onto highly doped p<sup>++</sup>-Si substrate with 170 and/or 290 nm thick thermally grown SiO<sub>2</sub> layer. Using electron-beam lithography, metallic source and drain contacts were defined on to opposite ends of a selected ZS using a two-step lithography process. In the first step, high work function metal (Pt;  $W = 6.1$  eV) was defined as the source contact. Accordingly, the drain contact was employed with a low work function metal (Ti;  $W = 4.33$  eV), in the step. For the present investigation, several devices were fabricated with various channel lengths (L) ranging from 1 to 10  $\mu\text{m}$ . All electrical assessment of the fabricated ZS SGTs/FET were carried using a Cascade Microtech Summit 11k probe station with single source measure unit (2636A by Keithley Instruments) under dark ambient conditions.

## Conclusion

To conclude, the present work has successfully demonstrated the fabrication and electrical characterization of high performance Pt/n-ZnO SGT devices based on single-crystalline ZnO sheets. The Pt/n-ZnO diode demonstrated low reverse leakage current of around 25 nA, with a rectification ratio greater than 100 at  $V_{\text{DS}} = +5$  V. Assessment of the field-effect transport characteristics of the fabricated SGT device revealed exceptionally low saturation voltages and 1000 times higher gain (at  $V_{\text{DS}} = 2$  V) compared to an identical ZS FET devices. The investigated SGT device is expected to be useful in applications where high output impedance, good current uniformity and stability are required, such as in driver transistors in emissive pixel circuits. We envisage that the present ZS SGT device may offer practical solutions to realise high performance low-power electronic device based on ZnO sheets.

## References

- Lu, W. & Lieber, C. M. Nanoelectronics from the bottom up. *Nat. Mater.* **6**, 841–850 (2007).
- Dasgupta, N. P. *et al.* 25th anniversary article: Semiconductor nanowires - Synthesis, characterization, and applications. *Adv. Mater.* **26**, 2137–2183 (2014).
- Avouris, P. Graphene: Electronic and photonic properties and devices. *Nano Lett.* **10**, 4285–4294 (2010).
- Meric, I. *et al.* Current saturation in zero-bandgap, top-gated graphene field-effect transistors. *Nat. Nanotechnol.* **3**, 654–659 (2008).
- Taniguchi, T., Yamaguchi, K., Shigeta, A., Matsuda, Y. & Hayami, S. Enhanced and Engineered d 0 Ferromagnetism in Molecularly-Thin Zinc Oxide Nanosheets. *Adv. Funct. Mater.* **23**, 3140–3145 (2013).
- Tang, Q., Li, Y., Zhou, Z., Chen, Y. & Chen, Z. Tuning electronic and magnetic properties of wurtzite ZnO nanosheets by surface hydrogenation. *ACS Appl. Mater. Interfaces* **2**, 2442–7 (2010).
- Eda, G. & Maier, S. A. Two-dimensional crystals: Managing light for optoelectronics. *ACS Nano* **7**, 5660–5665 (2013).
- Yin, Z. *et al.* Single-Layer MoS<sub>2</sub> Phototransistors. *ACS Nano* **6**, 74–80 (2012).
- Cho, K. *et al.* Electric stress-induced threshold voltage instability of multilayer MoS<sub>2</sub> field effect transistors. *ACS Nano* **7**, 7751–8 (2013).
- Lembke, D. & Kis, A. Breakdown of high-performance monolayer MoS<sub>2</sub> transistors. *ACS Nano* **6**, 10070–5 (2012).
- Radisavljevic, B., Whitwick, M. B. & Kis, A. Integrated circuits and logic operations based on single-layer MoS<sub>2</sub>. *ACS Nano* **5**, 9934–8 (2011).
- Likovitch, E. M., Russell, K. J., Petersen, E. W. & Narayanamurti, V. Weak localization and mobility in ZnO nanostructures. *Phys. Rev. B* **80**, 245318 (2009).



13. Dahiya, A. S. *et al.* Zinc oxide sheet field-effect transistors. *Appl. Phys. Lett.* **107**, 033105 (2015).
14. Liu, Z. *et al.* Synthesis, Anion Exchange, and Delamination of Co–Al Layered Double Hydroxide: Assembly of the Exfoliated Nanosheet/Polyanion Composite Films and Magneto-Optical Studies. *J. Am. Chem. Soc.* **128**, 4872–4880 (2006).
15. Hu, L., Ma, R., Ozawa, T. C. & Sasaki, T. Exfoliation of Layered Europium Hydroxide into Unilamellar Nanosheets. *Chem. - An Asian J.* **5**, 248–251 (2010).
16. Qiu, J., Guo, M. & Wang, X. Electrodeposition of hierarchical ZnO nanorod-nanosheet structures and their applications in dye-sensitized solar cells. *ACS Appl. Mater. Interfaces* **3**, 2358–67 (2011).
17. Xiao, Y. *et al.* Highly enhanced acetone sensing performances of porous and single crystalline ZnO nanosheets: high percentage of exposed (100) facets working together with surface modification with Pd nanoparticles. *ACS Appl. Mater. Interfaces* **4**, 3797–804 (2012).
18. Chen, S. J. *et al.* Structural and Optical Properties of Uniform ZnO Nanosheets. *Adv. Mater.* **17**, 586–590 (2005).
19. Kim, K.-H. *et al.* Piezoelectric two-dimensional nanosheets/anionic layer heterojunction for efficient direct current power generation. *Sci. Rep.* **3**, 2013 (2013).
20. Ju, S. *et al.* Low operating voltage single ZnO nanowire field-effect transistors enabled by self-assembled organic gate nanodielectrics. *Nano Lett.* **5**, 2281–2286 (2005).
21. Nasr, B. *et al.* High-Speed, Low-Voltage, and Environmentally Stable Operation of Electrochemically-Gated Zinc Oxide Nanowire Field-Effect Transistors. *Adv. Funct. Mater.* **23**, 1750–1758 (2012).
22. Ma, A. M. *et al.* Zinc oxide thin film transistors with Schottky source barriers. *Solid. State. Electron.* **76**, 104–108 (2012).
23. Ma, A. M. *et al.* Schottky barrier source-gated ZnO thin film transistors by low temperature atomic layer deposition. *Appl. Phys. Lett.* **103**, 253503 (2013).
24. Opoku, C. *et al.* Fabrication of field-effect transistors and functional nanogenerators using hydrothermally grown ZnO nanowires. *RSC Adv.* **5**, 69925–69931 (2015).
25. Opoku, C. *et al.* Fabrication of high performance field-effect transistors and practical Schottky contacts using hydrothermal ZnO nanowires. *Nanotechnology* **26**, 355704 (2015).
26. Shannon, J. M. & Gerstner, E. G. Source-Gated Thin-Film Transistors. *IEEE Electron Device Lett.* **24**, 405–407 (2003).
27. Sporea, R. A., Trainor, M. J., Young, N. D., Shannon, J. M. & Silva, S. R. P. Source-gated transistors for order-of-magnitude performance improvements in thin-film digital circuits. *Sci. Rep.* **4**, 4295 (2014).
28. Balon, F. & Shannon, J. M. Analysis of Schottky barrier source-gated transistors in a-Si:H. *Solid. State. Electron.* **50**, 378–383 (2006).
29. Xu, X., Sporea, R. & Guo, X. Source-Gated Transistors for Power- and Area-Efficient AMOLED Pixel Circuits. *J. Disp. Technol.* **10**, 928–933 (2014).
30. Shannon, J. M., Sporea, R. A., Georgakopoulos, S., Shkunov, M. & Silva, S. R. P. Low-Field Behavior of Source-Gated Transistors. *IEEE Trans. Electron Devices* **60**, 2444–2449 (2013).
31. Yang, W. F. *et al.* Temperature Dependence of Carrier Transport of a Silicon Nanowire Schottky-Barrier Field-Effect Transistor. *IEEE Trans. Nanotechnol.* **7**, 728–732 (2008).
32. Tan, E. J. *et al.* Nickel-silicided Schottky junction CMOS transistors with gate-all-around nanowire channels. *IEEE Electron Device Lett.* **29**, 902–905 (2008).
33. Balon, F., Shannon, J. M. & Sealy, B. J. Modeling of high-current source-gated transistors in amorphous silicon. *Appl. Phys. Lett.* **86**, 1–3 (2005).
34. Sporea, R. A. *et al.* Performance trade-offs in polysilicon source-gated transistors. *Solid State Electron.* **65–66**, 246–249 (2011).
35. Cheng, H. M. *et al.* Enhanced resonant Raman scattering and electron-phonon coupling from self-assembled secondary ZnO nanoparticles. *J. Phys. Chem. B* **109**, 18385–18390 (2005).
36. Allen, M. W. & Durbin, S. M. Influence of oxygen vacancies on Schottky contacts to ZnO. *Appl. Phys. Lett.* **92**, 122110 (2008).
37. Das, S. N. *et al.* Fabrication and Characterization of ZnO Single Nanowire-Based Hydrogen Sensor. *J. Phys. Chem. C* **114**, 1689–1693 (2010).
38. Sze, S. M. & Ng, K. K. *Physics of Semiconductor Devices 3rd edition*, Ch. 3, 146–166 (New York: Wiley-Interscience 2007).
39. Choi, S., Choi, C., Kim, J., Jang, M. & Choi, Y. Analysis of Transconductance (gm) in Schottky-Barrier MOSFETs. *IEEE Trans. Electron Devices* **58**, 427–432 (2011).
40. Zhang, A., Zhao, X.-R., Duan, L.-B., Liu, J.-M. & Zhao, J.-L. Numerical study on the dependence of ZnO thin-film transistor characteristics on grain boundary position. *Chinese Phys. B* **20**, 057201 (2011).
41. Sze, S. M. & Ng, K. K. *Physics of Semiconductor Devices 3rd edition*, Ch. 6, 303–307 (New York: Wiley-Interscience 2007).
42. Sporea, R. A., Trainor, M. J., Young, N. D., Shannon, J. M. & Silva, S. R. P. Intrinsic gain in self-aligned polysilicon source-gated transistors. *IEEE Trans. Electron Devices* **57**, 2434–2439 (2010).
43. Appenzeller, J., Member, S., Knoch, J. & Björk, M. T. Toward Nanowire Electronics. *IEEE Trans. Electron Devices* **55**, 2827–2845 (2008).
44. Sporea, R. A., Overy, M., Shannon, J. M. & Silva, S. R. P. Temperature dependence of the current in Schottky-barrier source-gated transistors. *J. Appl. Phys.* **117**, 184502 (2015).
45. Sporea, R. A., Trainor, M., Young, N., Shannon, J. M. & Silva, S. R. P. Temperature Effects in Complementary Inverters Made With Polysilicon Source-Gated Transistors. *IEEE Trans. Electron Devices* **62**, 1498–1503 (2015).

## Acknowledgements

This work was financially supported by Region Centre (France) through the project APR-CeZnO and by National Research Agency funding (ANR-14-CE08-0010-01).

## Author Contributions

A.S.D. and N.C. designed the experiments. A.S.D. performed the synthesis and majority of structural/morphological analysis of the ZnO sheets (ZS). A.S.D. and C.O. fabricated ZS based FETs and SGTs. A.S.D. carried out all electrical characterizations of fabricated transistors. F.C. prepared the TEM lamellas and performed HRTEM characterization. R.A.S. performed simulations for ZS SGT devices. The drafting of the manuscript has been done by A.S.D., B.S. and C.O. D.A., G.P.V. and N.C. did critical revisions of the manuscript. All authors have read and approved the final manuscript.

## Additional Information

**Competing financial interests:** The authors declare no competing financial interests.

**How to cite this article:** Dahiya, A. S. *et al.* Single-crystalline ZnO sheet Source-Gated Transistors. *Sci. Rep.* **6**, 19232; doi: 10.1038/srep19232 (2016).



This work is licensed under a Creative Commons Attribution 4.0 International License. The images or other third party material in this article are included in the article's Creative Commons license, unless indicated otherwise in the credit line; if the material is not included under the Creative Commons license, users will need to obtain permission from the license holder to reproduce the material. To view a copy of this license, visit <http://creativecommons.org/licenses/by/4.0/>